Contribution from the Department of Chemistry,
Princeton University, Princeton, New Jersey 08544

Optical Absorption and Luminescence Spectra of Rh^{3+}-Doped Cs_2NaMCl_6 (M = Y, In, Sc) Single Crystals

S. Catherine Weaver† and Donald S. McClure*

Received November 19, 1991

The optical absorption and emission properties of Rh^{3+} in Cs_2NaMCl_6 (M = Y, In, Sc) and of Ir^{3+} (M = In) were studied and compared to the more highly resolved spectra of the PtF_6^{2-} ion. Single crystals were grown by the Bridgeman method and characterized by X-ray diffraction. The emission decay time is 22 ms for Rh^{3+} and 4.8 ms for Ir^{3+}, but nonradiative quenching occurs above 150 K in the three host lattices. The observed temperature dependence gave values for the promoting mode and accepting modes in agreement with the broad spectral intervals observed and with analogous PtF_6^{2-} modes. The energy gap between absorption and emission has been explained in terms of the promoting modes and the S-factors of the combining states. A crystal field calculation including spin–orbit coupling is used to fit the observed levels and show where unobserved ones must lie.

Introduction

The $RhCl_6^{3-}$ ion has a t_{2g}^6 ground state and its low-lying excited states belong to the $t_{2g}^5e_g$ configuration. It is isoelectronic with a large number of other octahedral complexes having strong ligand fields. These include complexes of the heavy transition metal ions such as PtF_6^{2-} discussed in the preceding article.[1] Their optical spectra are all similar since they have weak $^1A_{1g} \rightarrow {}^3T_{1g}$, $^3T_{2g}$ spin-forbidden transitions at low energy followed by two spin-allowed transitions $^1A_{1g} \rightarrow {}^1T_{1g}$, $^1T_{2g}$.

Although these spectra are understood in broad outline, certain details are left unresolved after a cursory spectroscopic study. The triplet states are weakly absorbing, and the lowest one is often evidenced only by its luminescence. Therefore, a "gap" between the beginning of luminescence and the beginning of absorption is reported.

In the case of PtF_6^{2-} in the host crystal Cs_2GeF_6 it was possible to abolish the reported gap and locate the position of a zero-phonon line corresponding to a pure electronic transition between $^1A_{1g}$ and $^3T_{1g}(E)$, the lowest multiplet component. (Hereafter we omit subscript g from electronic term symbols.) The coupling between the molecular complex and the lattice was shown to be of intermediate strength since molecular vibrations were resolved but lattice vibrations were not. That is, the lattice mode distribution did not simply display the one-phonon density of states but was more extensive and showed no discrete features. One- and two-photon spectroscopy was used to discern fine structure in the dilute crystalline solutions at low temperatures.

The work presented here uses three elpasolite structure host crystals: Cs_2NaMCl_6 (M = Y, In, Sc). The MCl_6 octahedra are uncoupled from each other as in the case of Cs_2GeF_6 used for tetravalent ions. The structure of the crystal is illustrated in Figure 1. Thus, the $RhCl_6^{3-}$ octahedron is in the same type of environment as PtF_6^{2-} in Cs_2GeF_6. This strictly cubic environment reduces the spectral complexity compared to less symmetrical ones.

We have measured one-photon absorption, excitation and emission spectra for these crystals. Two-photon spectroscopy has not been done, partly because of the extra difficulty of working in the infrared and partly because the one-photon results suggested that not much more would be learned. We have been able to locate the probable position of the zero-phonon line to within about 100 cm^{-1}. The positions of the triplet states have been located with the combined help of the experimental data and a d^6 crystal field calculation. The much reduced fine structure in $RhCl_3^{3-}$ compared to PtF_6^{2-} prevented a detailed analysis of the transition mechanism, but our measurements of the temperature dependence of the emission lifetime and the quantum yield have partly compensated for this lack.

The data for Ir^{3+} are not as good as for Rh^{3+}, but are still interesting. It is also worth noting the work of Schatz et al. on Ir^{4+} in Cs_2ZrCl_6, where the Ir^{4+} also exists as an octahedral ion.[2] These spectra are much better resolved than the Ir^{3+} spectra, presumably because the $IrCl_6^{2-}$ octahedron is much less coupled to the lattice than the $IrCl_6^{3-}$ octahedron. This is also true of PtF_6^{2-}, which we use for comparison.

Experimental Section

Synthesis. The elpasolite powders were prepared using method E described by Morss et al.[3] Stoichiometric amounts of the metal chlorides (CsCl (Aldrich 99.9%), NaCl (EM Reagents Suprapur), and $YCl_3 \cdot 6H_2O$ (Aldrich 99.9%), $InCl_3$ (Aesar 99.999%), or $ScCl_3 \cdot 6H_2O$ (Strem 99.9%)) were dissolved in concentrated HCl (Mallinckrodt AR); gentle heating was required to fully dissolve the reagents, and this solution was evaporated to dryness. The resultant powders were heated while under vacuum to remove any residual water.

X-ray powder patterns were obtained to confirm the face-centered cubic nature of the products. Small amounts of residual CsCl and NaCl were identified, but no other unidentifiable lines were observed. The lattice parameters determined for Cs_2NaYCl_6 (a = 10.74(2) Å), $Cs_2NaInCl_6$ (a = 10.50(4) Å), and $Cs_2NaScCl_6$ (a = 10.47(4) Å), are the same within error limits as those reported by Morss et al.[3]

Single crystals of the elpasolites doped with Rh or Ir were grown in sealed quartz crucibles using the Bridgeman method. After the host salt is dried under vacuum, it is mixed with the dopant, anhydrous $RhCl_3$ or $IrCl_3$ (Aldrich 98%), in an Ar atmosphere drybox. The mixture is replaced in the quartz crucible and sealed under vacuum.

The average temperature gradient in the Bridgeman furnace was about 30 °C/cm, and the ideal lowering speed through this gradient was determined to be 3.0 mm/h which corresponds to about 9 °C/h. The temperature in the hot zone was set to 860 °C for Cs_2NaYCl_6, 700 °C for $Cs_2NaInCl_6$, and 1050 °C for $Cs_2NaScCl_6$. When the crucible was lowered to the bottom of the furnace, the heat was turned off, and the crystal was allowed to cool slowly to room temperature.

The crystals obtained were a rosy pink color about 2 cm long by 1 cm in diameter. Samples for the spectroscopic measurements were cleaved from the boules; however, the crystals do not cleave along definite planes. Due to their hygroscopic nature, the crystals must be kept in a dry atmosphere. X-ray diffraction pictures were taken of each sample to verify that they were single crystals.

Spectroscopy. The optical experiments involved the measurement of absorption, emission, and excitation spectra, typically at liquid-helium temperatures. The various experimental setups and cryogenic equipment that were used are described here.

Absorption spectra were recorded with a Cary 14R spectrometer with the crystals mounted in a Pope Scientific quartz dewar which fit inside the Cary sample compartment. The crystals were cooled by immersion in liquid helium; the lambda point could be obtained by pumping on the helium vapor. For all the other low-temperature experiments, the crystals were held in a Janis (10DT) liquid helium cryostat, and a Lake Shore cryogenics temperature controller (DRC 80C) monitored the temperature with a silicon diode temperature sensor (DT-470 series) mounted on the sample holder. The temperature was adjusted by varying the helium gas

† Present address: Institute for Defense Analyses, 1801 N. Beauregard St., Alexandria, VA 22311.

(1) Campochiaro, C.; McClure, D. S.; Patterson, H. H. *Inorg. Chem.* preceding paper in this issue.
(2) Yeakel, W. C.; Schatz, P. N. *J. Chem. Phys.* **1974**, *61*, 441.
(3) Morss, L. R.; Siegal, M.; Stenger, L.; Edelstein, N. *Inorg. Chem.* **1970**, *9*, 1771.

0020-1669/92/1331-2814$03.00/0

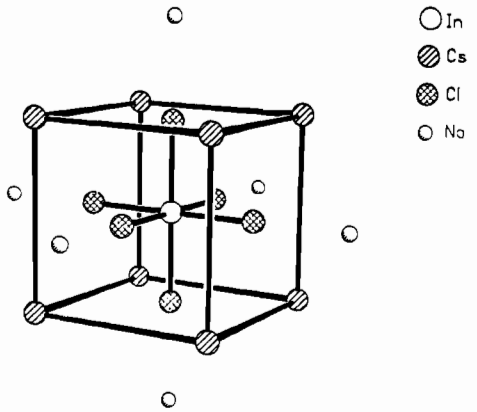

Figure 1. X-ray crystal structure of $Cs_2NaInCl_6$. The Rh^{3+} ion substitutes for the In^{3+} ion at a site of perfect octahedral symmetry.

flow rate past the sample, and the experiments were performed at a constant temperature around 5 K.

The Rh^{3+} emission was excited with a nitrogen laser-pumped dye laser (Molectron UV24-DLII) lasing at 554 nm (Rhodamine 560 laser dye) and operating at 10 Hz (10-ns pulse width). This wavelength excited the low-energy side of the $^1A_1 \rightarrow {}^1T_1$ band of the Rh^{3+}-doped materials studied. The Ir^{3+} emission was excited at 440 nm (Coumarin 440 laser dye).

The sample emission was collected and passed through a McPherson 2m, $f/17$ monochromator equipped with an IR grating (300 lines/mm) blazed at 2 μm. The linear dispersion of this grating is 16 Å/mm at the exit slit. This corresponds to about 6 cm^{-1} resolution for 400-μm slit widths, the narrowest widths used in these experiments. The monochromator wavelength was calibrated with an Ar pen lamp, and the calibration scan was repeated periodically during the emission experiments and observed to be reproducible within 1 cm^{-1}.

The dispersed emission impinged on a liquid-nitrogen-cooled Ge detector (North Coast EO-817L). The Ge detector has a detectivity near that of a photomultiplier tube, is operated at −250 V bias, has an integrated preamplifier, and outputs a low impedance voltage which is connected to a gated boxcar averager (Stanford Research Systems SR 250) for signal collection. The spectra are uncorrected for the detector or monochromator response curve.

Emission decay times were measured as a function of temperature from 4 to 300 K. The sample temperature was varied with the North Shore temperature controller which was connected to a heater wire wrapped around the sample holder. The samples were excited as above, and the emission was detected with an S-1 PMT (Amperex, 1600 V) placed directly in front of the dewar window with an Si filter to block the exciting radiation. It was desirable to use a PMT (terminated to 50 Ω) instead of the Ge detector in order to determine the emission lifetime without the interference of the detector response curve. The signal from the PMT is fed into a digitizing oscilloscope (HP 54111D) and averaged for 64 laser shots.

One-photon laser excitation spectra were taken to find the origin of the triplet absorption that is too weak to be observed in the Cary absorption spectra. A Nd:YAG (Quantel) pumped dye laser (Lambda-Physik) was the excitation source. With this source, pulse energies sufficient for one-photon absorption could be obtained for wavelengths out to 950 nm. Typical pulse energies were 1-2 mJ for 10-ns, 10-Hz pulses. The Ge detector was placed directly in front of the dewar window, at 90° to the exciting light, with an Si filter and several glass cutoff filters (Schott, RG-1000) to block the exciting radiation. The signal was fed to a gated boxcar integrator. The dye laser wavelength was calibrated in a separate experiment by the optogalvanic method. The detector output was always referenced to the pulse energy.

Results

The absorption, emission and excitation spectra of Rh^{3+} in the three hosts and of Ir^{3+} in $Cs_2NaInCl_6$ are shown in Figures 2 and 3. Two broad peaks are observed in absorption which are assigned as the spin-allowed $^1A_1 \rightarrow {}^1T_1$ transition at lower energy and the $A_1 \rightarrow {}^1T_2$ transition at higher energy. The 2 K absorption spectra show a vibrational progression on the $^1T_1$ band. The progression energy is about 290 cm^{-1} for Rh^{3+} in all three hosts. At room temperature, the bands are broadened and the temperature dependence indicates the vibronic nature of the transition moment. A third, higher energy peak is observed for the Y-host. The absorption spectral data are summarized in Table I.

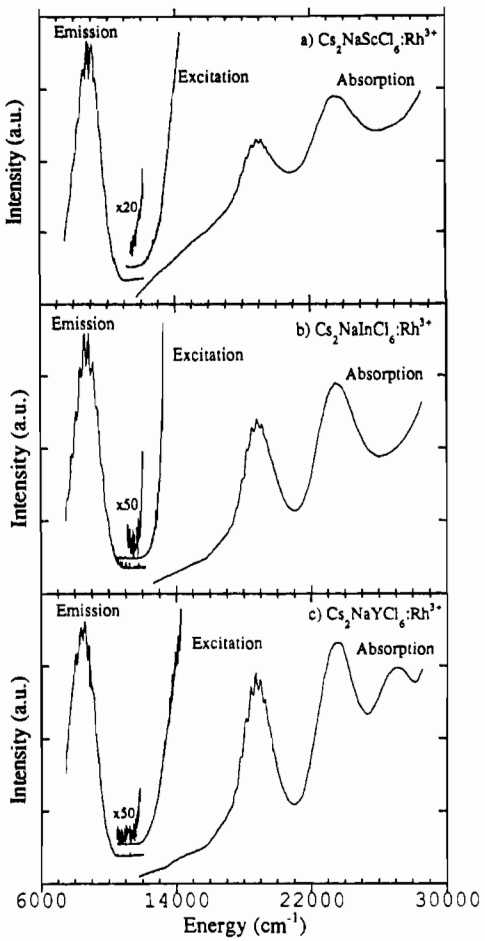

Figure 2. Emission, excitation, and absorption spectra of Rh^{3+}-doped (a) $Cs_2NaScCl_6$, (b) $Cs_2NaInCl_6$, and (c) Cs_2NaYCl_6 at liquid-helium temperatures. The actual absorption coefficients (cm^{-1}) at the peak of the $^1T_{1g}$ band are (a) 4.9, (b) 9.0, and (c) 4.5.

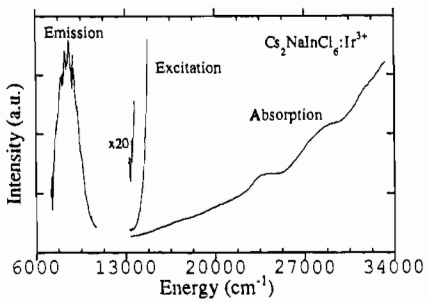

Figure 3. Emission, excitation, and absorption spectra of Ir^{3+}-doped $Cs_2NaInCl_6$ at liquid-helium temperatures.

Table I. Summary of Absorption and Excitation Spectral Data[a]

	$Cs_2NaMCl_6:M'$			
	$Y:Rh^{3+}$	$In:Rh^{3+}$	$Sc:Rh^{3+}$	$In:Ir^{3+}$
excitation origin (±100)	11600	11800	11900	13500
$^1T_{1g}$ peak	18700	18900	18900	23900
$h\nu_{accept}$	290	290	290	...
fwhm	2000	2000	2000	
$^1T_{2g}$ peak	23400	23500	23400	29000
fwhm	3000	3000	3000	
$10^{-18}N$, cm^{-3}	2.4	5.0	4.4	0.5 (160 ppm)
$10^{-3}f_s(^1T_{1g})$	3.5	3.5	2.1	

[a] All values are in wavenumbers (cm^{-1}).

The optical experiments were performed on crystals directly cleaved from their boules because it was found that cleaved faces were somewhat less hygroscopic than polished faces. However,

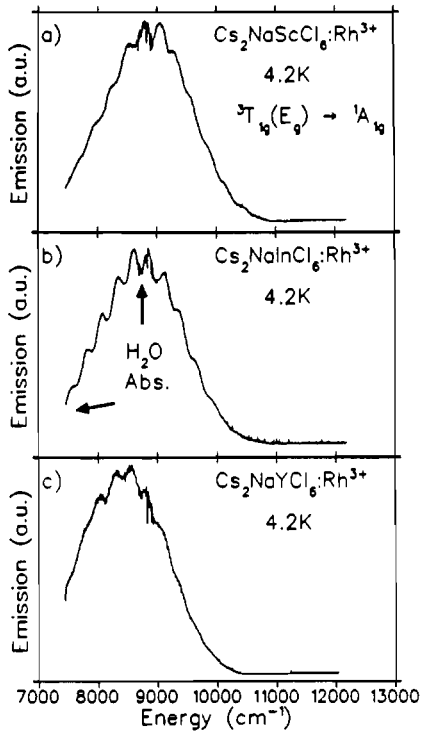

Figure 4. Detail of the emission spectra of Rh^{3+} in (a) $Cs_2NaScCl_6$, (b) $Cs_2NaInCl_6$, and (c) Cs_2NaYCl_6 at 4.2 K. The sharp features around 8800 cm^{-1} are due to water vapor absorption of the emission. Emission below 7500 cm^{-1} is also absorbed by water vapor. The excitation wavelength is 554 nm.

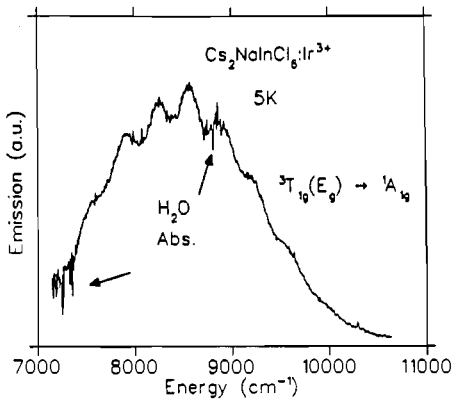

Figure 5. Detail of the emission spectrum of Ir^{3+} in $Cs_2NaInCl_6$ at 4.2 K. The sharp features around 8800 cm^{-1} are due to water vapor absorption of the emission. Emission below 7500 cm^{-1} is also absorbed by water vapor. The excitation wavelength is 440 nm.

light scattering was still a problem for the absorption measurements. The strongly sloping baselines in the absorption spectra are indicative of the poor optical quality of these crystals. Furthermore, data gathering further into the UV was precluded by the sloping baseline and probably the beginning of chloride to metal charge-transfer bands.

Luminescence from the Rh^{3+} ion in all three host crystals is observed in the near-infrared region as shown in Figure 2 and in more detail in Figure 4. The Ir^{3+} emission spectrum is shown in more detail in Figure 5. Ligand field calculations give the E component as the lowest energy spin–orbit level of $^3T_1$. The emission band is therefore assigned as the $^3T_1(E) \rightarrow {}^1A_1$ transition. Furthermore, ligand field theory predicts that, for octahedral symmetry, $E \rightarrow A_1$ transitions are strictly forbidden as magnetic dipole transitions; this is corroborated by the long emission lifetime of nearly 22 ms for Rh^{3+} and 5 ms for Ir^{3+} at liquid-helium temperatures. A vibronic progression is present on the emission band similar to the one observed on the $^1T_1$ absorption band. The average progression energy for Rh^{3+} is 260–270 cm^{-1} and for Ir^{3+} is about 350 cm^{-1}. The sharp features around 8800 cm^{-1} are due to absorption of the emission by atmospheric water vapor. Also, the spectra are not shown for energies less than 7500 cm^{-1} due to a large water absorption band in that region. The emission spectral data are summarized in Table II.

Table II. Summary of Emission Spectral Data (cm^{-1})

	$Cs_2NaMCl_6:M'$			
	$Y:Rh^{3+}$	$In:Rh^{3+}$	$Sc:Rh^{3+}$	$In:Ir^{3+}$
emission onset	10500	10800	11000	11000
peak	8450	8740	8800	8600
E_{gap} (±100)	1100	1000	900	2500
fwhm	1700	1600	1700	1900
$h\nu_{accept}$	260	270	270	
$^3T_{1g}(E_g)$ origin[a]	11050	11300	11450	12050
$^3T_{1g}(E_g)$ peak[b]	13650	13850	14020	14450

[a] Estimated to be at the middle of the energy gap. [b] Peak energy is estimated to be the same energy above the origin as emission peak is below the origin.

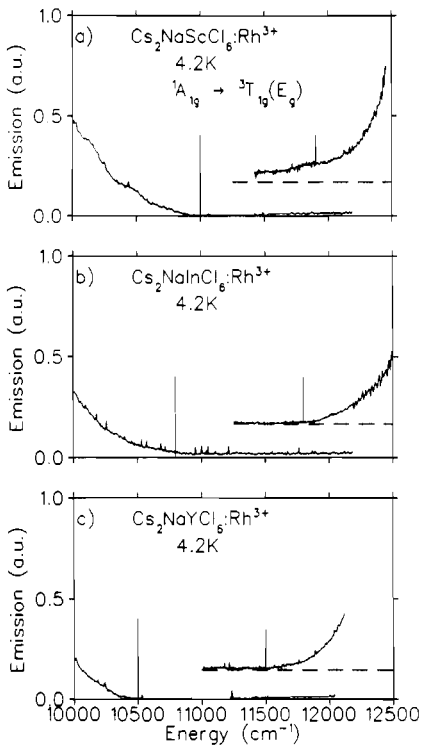

Figure 6. One-photon laser excitation spectra of Rh^{3+} in (a) $Cs_2NaScCl_6$, (b) $Cs_2NaInCl_6$, and (c) Cs_2NaYCl_6 at 4.2 K. The beginning of the emission band for each compound is also shown, and the excitation spectra are offset for clarity. The onset of excitation and emission are indicated by the vertical lines. The zero-phonon origins are estimated to be halfway in between the vertical lines.

One-photon laser excitation spectra of Rh^{3+} and Ir^{3+} were taken starting at the highest energy point of the emission and continuing for about 3000 cm^{-1}. These spectra are also shown in Figures 2 and 3. Figure 6 shows the excitation spectra of Rh^{3+} in the three crystals in more detail together with the estimated location of the zero-phonon line. The latter has been taken as the midpoint between the "onset" of emission and the "onset" of excitation. This energy separation or "gap" is shown between the two vertical lines. Both of these onset points are quite arbitrary since they depend on the sensitivity of the detectors and on the strength of the excitation. The sharp rise in both excitation and emission, however, gives some validity to these estimates. The vibrational structure of the emission band and the estimated position of the zero-phonon line can be used together to determine the Huang–Rhys factor for the fluorescence transition. The excitation data obtained for $Cs_2NaScCl_6:Rh^{3+}$ is of poorer quality. The scattered light background is higher, and it was more difficult to piece together the scan regions of the different laser dyes. The slight rise in the excitation spectrum before the vertical line in Figure 6a is an

Table III. Crystal Field Parameters and Calculated and Observed Energy Levels for $Cs_2NaInCl_6:Rh^{3+}$

param	value, cm^{-1}
Dq	2035
B	330
C	2220
ζ	700

		energy, cm^{-1}	
		obs	calc
$^1A_{1g}$		0	0
$^3T_{1g}$	$\Gamma_3(E)$	13850[a]	13856
	$\Gamma_5(T_2)$		13941
	$\Gamma_4(T_1)$		14313
	$\Gamma_1(A_1)$		14658
$^3T_{2g}$	$\Gamma_4(T_1)$		16272
	$\Gamma_3(E)$		16459
	$\Gamma_5(T_2)$		16830
	$\Gamma_2(A_2)$		17054
$^1T_{1g}$	$\Gamma_4(T_1)$	18900	18916
$^1T_{2g}$	$\Gamma_5(T_2)$	23500	23541

[a] See Table II.

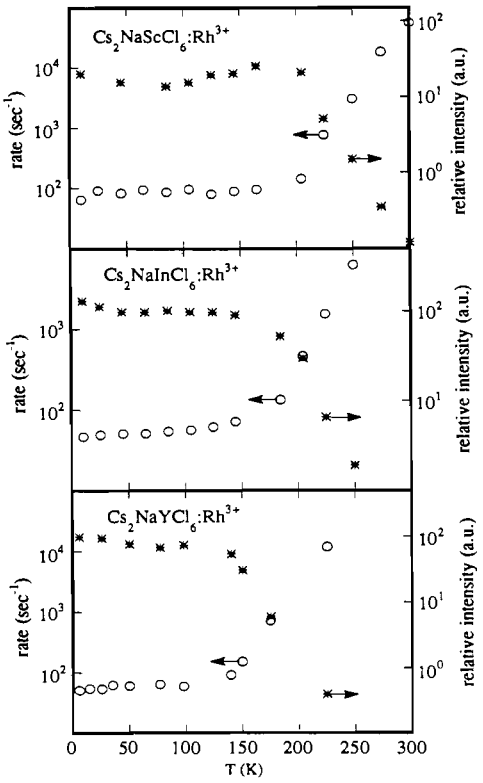

Figure 7. Emission decay rates and relative intensities versus temperature for Rh^{3+} in (a) $Cs_2NaScCl_6$, (b) $Cs_2NaInCl_6$, and (c) Cs_2NaYCl_6.

artifact due to the laser dye tuning curve as is the slight decrease at the beginning of the excitation spectrum in Figure 2b.

The excitation spectra shown in Figures 2 and 3 extend to about 14000 cm^{-1}; however, no peaks are observed, only a continual increase in signal. This sharp increase in signal stresses the dynamic range of the experiment at higher energies. The Ge detector has only one sensitivity level, and the use of neutral density filters caused unwanted etalon patterns (e.g., see Figure 2c and Figure 6b. The spectra in Figure 6 extend only to 12000 cm^{-1}, but the most important result is evident, the onset of excitation. The Ir^{3+} spectra are not shown in expanded detail, and the reason for this is discussed in more detail below.

Further information on the optical properties of Rh^{3+}-doped elpasolites is obtained from the temperature dependence of the emission lifetime. The decay curves for the Rh^{3+} emission could be fit to a single exponential for all the systems studied at all temperatures. The decay rates obtained from the single exponential and the relative intensity are plotted versus temperature

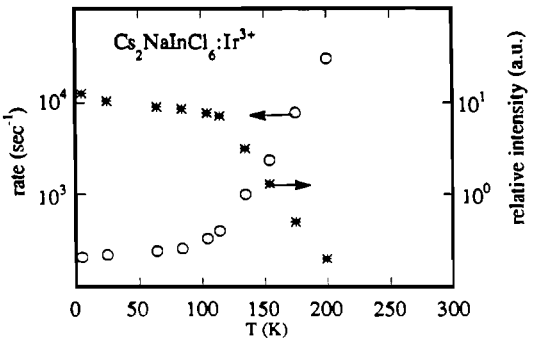

Figure 8. Emission decay rates and relative intensities versus temperature for Ir^{3+} in $Cs_2NaInCl_6$.

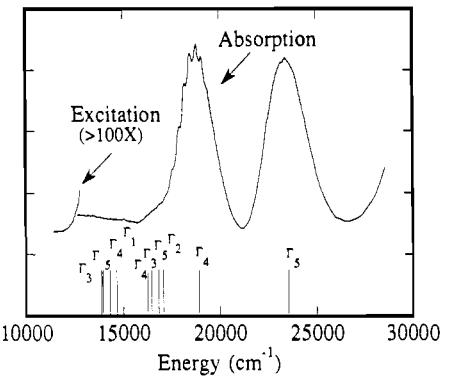

Figure 9. Absorption and one-photon excitation spectra of $Cs_2NaInCl_6:Rh^{3+}$ at 2 K shown with the calculated level positions.

for Rh^{3+} in the three host crystals in Figure 7. Similar data obtained for the Ir^{3+} crystal are shown in Figure 8. Two distinct trends are apparent with an abrupt transition between them. Radiative transitions dominate at lower temperatures and are characterized by a small increase in the transition rate with increasing temperature due to thermal enhancement of the vibronic emission probability. The dramatic increase of the decay rate above 150 K with a corresponding decrease in relative intensity is indicative of the onset of nonradiative relaxation processes. These trends are discussed more quantitatively in the next section.

Discussion

A discussion of the spectroscopic results presented in the last section for Rh^{3+} in the chloride elpasolites Cs_2NaYCl_6, $Cs_2NaInCl_6$, and $Cs_2NaScCl_6$ and $Cs_2NaInCl_6:Ir^{3+}$ is presented here. The main difference between these three hosts is the "socket size" at the site of the dopant ion. All three of the host trivalent metal ions have larger ionic radii than the Rh^{3+} ion; the Rh^{3+}/M^{3+} ratios are 0.77, 0.85, and 0.91 for Y^{3+}, In^{3+}, and Sc^{3+}, respectively. The crystal field at the M^{3+} site is largest for the smallest socket size, i.e., for $Cs_2NaScCl_6$, and decreases for larger sites. The Tanabe–Sugano diagrams for d^6 ions show that the energies of the (t_2^5e) excited states all increase in a similar manner with an increasing crystal field. This trend can be seen in the emission and one-photon excitation spectra of Rh^{3+} in these three host crystals as discussed below. Furthermore, owing to the lanthanide contraction, the ionic radius of Ir^{3+} is not much larger than that of Rh^{3+}, 82 pm and 80.5 pm, respectively.

Absorption. The Rh^{3+} ion in octahedral coordination has a $^1A_1(t_2^6)$ ground state and the excited states are $^3T_1$, $^3T_2$, $^1T_1$, and $^1T_2$ (all t_2^5e). In the absorption spectra of Figure 2, the spin allowed singlet–singlet transitions are easily observed and assigned. The broad-band transitions have similar widths and peak energies for all three hosts, but the $^1T_{1g}$ band peaks are found at a slightly lower energy in the Cs_2NaYCl_6 host. The singlet absorption transitions are shifted to higher energy by about 5000 cm^{-1} or 20% for Ir^{3+}. This is a result of the increased crystal field splitting due to the change from 4d to 5d orbitals.

The concentration of Rh^{3+} and Ir^{3+} in the elpasolite crystals was determined by atomic absorption[4] and is listed in Table I.

Using this information, the oscillator strength for the singlet states can be estimated from the absorption bands

$$f_s = \left(\frac{2.303mc^2}{\pi Le^2}\right)\left(\frac{9n}{(n^2+2)^2}\right)\epsilon_{max}\Delta\bar{\nu} \qquad (1)$$

where e and m are the electron charge and mass, L is Avogadro's number, and the local field correction is included. ϵ_{max} is given by $\sigma L/(10^3)2.303$ where σ is the absorption cross section (α/N) and $\Delta\bar{\nu}$ is the fwhm given in Table I. The value of n is taken to be 1.3.[5] The oscillator strengths given in Table I are found to be on the order of 10^{-3}, which are in the expected range for spin-allowed, parity-forbidden d–d transitions. The low value for the $Cs_2NaScCl_6:Rh^{3+}$ crystal is probably due to experimental error in measuring the absorption coefficients. These crystals have poor optical quality and light scattering is a problem for the absorption measurements.

Emission. A more noticeable effect of the crystal field strength on the transition energies is observed in the luminescence spectra shown in Figures 4 and 5. The energy of the $^3T_1 \rightarrow {}^1A_1$ transition increases in the order Cs_2NaYCl_6, $Cs_2NaInCl_6$, and $Cs_2NaScCl_6$ as expected with the increasing crystal field strength. Comparing the ionic radius for Y^{3+} (104 pm), In^{3+} (94 pm), and Sc^{3+} (88.5 pm), we see that the size decreases by about twice as much from Y to In as from In to Sc. Accordingly, the peak energy of the emission band is seen to increase roughly twice as much between the Y host and the In host as between the In host and the Sc host. The $Cs_2NaInCl_6:Ir^{3+}$ emission spectrum is similar to that observed for $Cs_2NaInCl_6:Rh^{3+}$, although it is somewhat broader, and the peak is shifted to lower energy by 300 cm^{-1}.

The 4.2 K emission spectra show a vibrational progression similar to the 290 cm^{-1} progression observed in the absorption spectra, and the average progression energy is 260–270 cm^{-1}. The Ir^{3+} data indicate about 350 cm^{-1}. The emission progression energy appears to be lower than the absorption progression energy which is contrary to expectations since the excited state typically has weaker bonds with smaller force constants and thus reduced vibrational frequencies. It is possible that both a_{1g} and e_g modes may be involved in the relaxation processes and the observed progression energy is the average of these two modes giving a reduced value compared to the pure a_{1g} progression observed on the absorption band. The existence of Jahn–Teller activity resulting in an e_g-type progression has been identified in other d^6 ions,[6,7] and PtF_6^{2-} is one example.

The low-temperature decay times are in the millisecond range in agreement with a spin- and parity-forbidden transition. In fact, the measured lifetimes are near 20 ms for Rh^{3+} corroborating the assignment to the highly forbidden $^3T_1(E) \rightarrow {}^1A_1$ transition, and the radiative decay time is governed by the amount of triplet character mixed into the $^1A_1$ ground state wave functions through spin–orbit coupling. The oscillator strength for the emitting triplet state, f_t, can be estimated from the emission peak energy, $\bar{\nu}$, and lifetime, τ.

$$f_t = \frac{1.5}{\bar{\nu}^2\tau} \qquad (2)$$

The resulting f_t is approximately 1×10^{-6} for the three Rh^{3+} compounds, about 10^3 times smaller than f_s for the spin-allowed singlet transitions. It is understandable that the triplet transitions are only weakly seen in absorption with such a low value for the oscillator strength. The low-temperature emission lifetime is 4.8 ms for Ir^{3+}, giving an oscillator strength of about 4×10^{-6}. The shorter lifetime and larger oscillator strength is evidence that the emitting transition is more allowed for Ir^{3+}, and it must be due to larger spin–orbit coupling in the 5d ion.

One-Photon Excitation. The one-photon excitation spectra in Figure 6 do not show a sharp zero-phonon origin or a discernable vibronic origin. There are no significant one-photon electronic transition mechanisms for $^1A_{1g} \rightarrow {}^3T_{1g}(E)$. The S factor for the transition is large (see later), and inhomogeneous broadening is undoubtedly important here. All of these factors reduce the observability of the features of the excitation spectrum.

Since no sharp fine structure was observed in the Rh^{3+} or Ir^{3+} excitation spectra, the vibrational frequencies involved in the vibronic transitions cannot be directly assigned. However, average enabling and accepting mode frequencies can be determined from the temperature dependence of the lifetime and compared to the spectral data. (This is discussed below.)

The excitation origin listed in Table I is the lowest energy where signal is observed. There is about a 1000-cm^{-1} gap between the onset of observed excitation and emission. The true origin (zero-phonon energy) is assumed to be about halfway inbetween the two energies. The Ir^{3+} spectra shown in Figure 3 indicate the onset of excitation near 13 500 cm^{-1} while the onset of emission is near 11 000 cm^{-1}. This corresponds to an energy gap of 2500 cm^{-1}. The larger gap in the Ir^{3+} spectrum is presumably because of the low signal levels; thus, the onset of excitation is observed at higher energies where a larger fraction of light is absorbed. Additionally, even though larger spin–orbit coupling makes the transition more allowed, the spin–orbit components are spread out over a larger energy region, resulting in a lower peak intensity.

Crystal Field Calculation. A complete level scheme calculation must include all the electron configurations involved in the octahedral d^6 complex, and thus some 210 wave functions must be considered. The perturbation matrix elements of the d-electron repulsion and static ligand field potential have been given by Tanabe and Sugano,[9] and the spin–orbit interaction matrices for the d^4 and d^6 configurations have been given by Schroeder.[10]

The energy levels calculated from these matrices depend on four parameters: the cubic field parameter $10Dq$, the Racah electrostatic parameters B and C, and the spin–orbit coupling parameter ζ. These parameters can be determined semiempirically by comparison with the experimental data; however, for the compounds in this study, the parameters can only be determined very approximately since only the two spin-allowed transitions can be assigned conclusively.

The energies for the $(t_{2g}^5e_g)$ triplet and singlet states in terms of $10Dq$, B, and C with that of $^1A_{1g}$ taken as 0 are given as

$^3T_1$	$10Dq - 3C$
$^3T_2$	$10Dq + 8B - 3C$
$^1T_1$	$10Dq - C$
$^1T_2$	$10Dq + 16B - C$

The transition energies of spin-allowed absorptions are given in Table I; the splitting between these bands determines a value for B. The splitting between the lowest energy singlet and triplet determines a value for C, but the peak energy of $^3T_1$ must be estimated. The triplet origin is taken to be in the middle of the energy gap between emission and excitation, and the peak is then estimated to be the same energy above the origin as the emission peak is below the origin. A value for the spin–orbit coupling parameter ζ is 1200 cm^{-1} in the free ion and will be reduced somewhat in the crystal.

A computer program is then used to compute the energies and compositions of all the states for the values of the parameters $10Dq$, B, C, and ζ as estimated from the above relations. The four parameters chosen fit the four spectral intervals if the $^3T_2$ assignment is applied to the weak shoulder at the low-energy side of the $^1T_1$ band.

A comparison with the Pt^{4+} spectrum is worth making at this point. In PtF_6^{2-} the $^3T_1(A_1)$ multiplet component is separated

(4) Schwarzkopf Microanalytical Laboratory, 56-19 37th Avenue, Woodside, NY 11377.
(5) Reber, C.; Güdel, H. U. *J. Lumin.* **1988**, *42*, 1. Reber, C.; Güdel, H. U.; Meyer, G.; Schleid, T.; Daul, C. A. *Inorg. Chem.* **1989**, *28*, 3249. Reber, C.; Güdel, H. U. *J. Lumin.* **1990**, *47*, 7.
(6) Laurent, M. P.; Patterson, H. H.; Pike, W.; Engstrom, H. *Inorg. Chem.* **1981**, *20*, 372.
(7) Hakamata, K.; Urushiyama, A.; Kupka, H. *J. Phys. Chem.* **1981**, *85*, 1983.
(8) Griffith, J. S. *The Theory of Transition Metal Ions*; Cambridge University Press: 1961.
(9) Tanabe, Y.; Sugano, S. *J. Phys. Soc. Jpn.* **1954**, *9*, 753.
(10) Schroeder, K. A. *J. Chem. Phys.* **1962**, *37*, 2553.

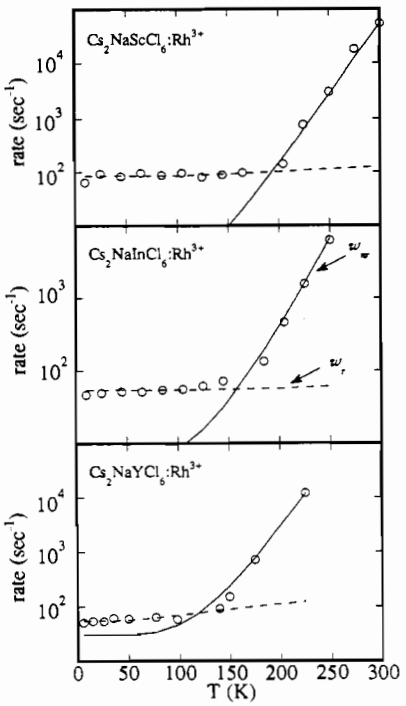

Figure 10. Calculated fits for the radiative, ω_r (broken line), and nonradiative, ω_{nr} (solid line), components of the temperature dependence of the decay rate for Rh^{3+} in (a) $Cs_2NaScCl_6$, (b) $Cs_2NaInCl_6$, and (c) Cs_2NaYCl_6. The data are plotted in open circles.

more from the three others (E, T_2, T_1) than in the case of $RhCl_6^{3-}$. Its prominence in the TP spectrum of Pt^{4+} suggests that one might see a significant difference between the OP and TP spectra of Rh^{3+} near 15 000 cm^{-1}. The $^3T_2$ spectrum was detected in the TP spectrum of PtF_6^{2-} only as a broad background just before the $^1T_1$ spectrum and it was even less noticeable in the OP spectrum. If the step-out in Rh^{3+} at 17 000 cm^{-1} is $^3T_2$, it may be more prominent in Rh^{3+} than in Pt^{4+} because there is less interference from $^3T_1(A_1)$. In Pt^{4+} the other three components of $^3T_1$ were relatively weak compared to the $^3T_1(A_1)$ component.

Radiative and Nonradiative Relaxation. The temperature dependence of the luminescence decay times and relative intensities shown in Figures 7 and 8 gives information about radiative and nonradiative relaxation processes involved in the Rh^{3+} and Ir^{3+} emission. The transition rate can be described by

$$\omega = \omega_{rad} + \omega_{hr} \tag{3}$$

where ω_{rad} is the radiative rate and ω_{nr} is the nonradiative rate. A model to rationalize the radiative decay behavior is based on the assumption that thermal equilibrium between the singlet and triplet excited states occurs on a much faster time scale than the deactivation to the ground state. It is further assumed that only the lowest spin–orbit component is involved in the luminescence process ($^3T_1(E) \rightarrow {}^1A_1$).

The radiative decay rate is then expressed as

$$\omega_{rad}(T) = \omega_{rad}(0) \coth (h\nu_{promote}/2kT) \tag{4}$$

with $\omega_{rad}(0)$ being the intrinsic radiative decay rate, and the coth factor describes the increase with temperature of the radiative rate as a result of the vibronic mechanism. $h\nu_{promote}$ corresponds to a weighted average of the t_{1u}, t'_{1u}, and t_{2u} enabling vibrational modes. The result of fitting eq 4 to the data for Rh^{3+} in the three hosts is shown as a broken line in Figure 10. The corresponding data and fits for Ir^{3+} are shown in Figure 11. Only the data below 150 K were used in fitting the radiative decay rate. The experimental data are well represented in the low-temperature range with two adjustable parameters $\omega_{rad}(0)$ and $h\nu_{promote}$. The best fits were obtained for $Cs_2NaInCl_6:Rh^{3+}$ and $Cs_2NaYCl_6:Rh^{3+}$ while the data for $Cs_2NaScCl_6:Rh^{3+}$ are more scattered. The signal/noise ratio measured for $Cs_2NaScCl_6:Rh^{3+}$ was smaller than for the other crystals; thus, there are larger experimental

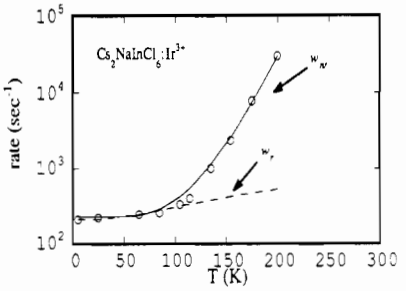

Figure 11. Calculated fits for the radiative, ω_r (broken line), and nonradiative, ω_{nr} (solid line), components of the temperature dependence of the decay rate for Ir^{3+} in $Cs_2NaInCl_6$. The data are plotted in open circles.

Table IV. Parameter Values for Radiative and Nonradiative Relaxation

	$Cs_2NaMCl_6:M'$			
	$Y:Rh^{3+}$	$In:Rh^{3+}$	$Sc:Rh^{3+}$	$In:Ir^{3+}$
E_{gap}, cm^{-1}	1100	1040	1020	2500
$h\nu_{promote}$, cm^{-1}	140	180	...	110
$\tau_r(0)$, ms	19.8	21.6	15.6	4.8
$h\nu_{accept}$, cm^{-1}	300	320	...	290
p_i	42	43	...	41

errors in the determination of the decay rates. As a result, the promoting mode frequency determined for this crystal is much larger than for the other two crystals and is not physically meaningful; the only conclusion that can be drawn is the average low-temperature radiative lifetime which is listed in Table IV. The results of the fits for the other three crystals are also listed in Table IV.

The luminescence decay rates and intensities indicate the onset of nonradiative relaxation above about 150 K in all the compounds. The most likely origin of this relaxation is from multiphonon processes. Many theoretical models for multiphonon relaxation have been proposed, but for the most part, the absolute value of the nonradiative rate is difficult to predict and only the temperature dependence can be adequately described.[11]

The approximation most often made is that only one vibrational (phonon) mode, the accepting mode, is responsible for the quenching process. This allows the correlation of the nonradiative relaxation behavior with other spectroscopic properties. Here we present a simple analysis that allows a qualitative comparison of the accepting mode with the observed E_{gap} and with vibrational data on other chloroelpasolites.

The analysis begins with a model developed by Riseberg and Moos for rare earth ions in crystals that involves the stimulated emission of phonons due to thermally populated phonon modes.[12] They found that the decay involves the emission of high-energy optical phonons and occurs in the lowest order permitted by energy conservation and cutoff in the phonon spectrum. The high-temperature nonradiative decay of Cr^{3+} in ruby and emerald could also be described this way.[13]

This model begins with the assumption that a given multiphonon decay process involves the emission of p_i phonons of equal energy involving the ith phonon mode. The nonradiative rate is then given by

$$\omega_{nr}(T) = [\omega_{nr}(0)](n_i + 1)^{p_i} \tag{5}$$

where n_i is the occupation number of the ith phonon mode and $\omega_{nr}(0)$ is the nonradiative relaxation rate at $T = 0$ K. The phonon modes become thermally populated as the temperature is increased and the multiphonon transition rate grows because of the stimulated emission of phonons. n_i is given by its Bose–Einstein average

$$n_i = [\exp(h\nu_i/kT) - 1]^{-1} \tag{6}$$

(11) DiBartolo, B. Ed. *Radiationaless Processes*; NATO ASI 1980; Plenum: New York, 1980.
(12) Riseberg, L. A.; Moos, H. W. *Phys. Rev.* **1968**, *174*, 429.
(13) Kisliuk, P.; Moore, C. A. *Phys. Rev.* **1967**, *160*, 307.

Table V. Summary of Vibrational Data (in cm^{-1}) for the Chloroelpasolites (Values from Ref 15)

compd	$\nu_1(a_{1g})$	$\nu_2(e_g)$	$\nu_3(t_{1u})$	$\nu_4(t_{1u})$	$\nu_6(t_{2u})$
$Cs_2NaScCl_6$	294		306		
$Cs_2NaInCl_6$	294		270		
Cs_2NaYCl_6	284	223	270		
$Cs_2NaScCl_6:Mo^{3+}$	310	270	295	150	115
$Cs_2NaScCl_6:Cr^{3+}$	315	270	300	150	110

	$h\nu_{accept}$	$h\nu_{promote}$
$Cs_2NaInCl_6:Rh^{3+}$	320	180

and ν_i is the effective accepting-mode frequency. This must be the highest frequency mode to which there is appreciable coupling; further, ω_{nr} is an extremely sensitive function of the number p of phonons required to bridge the energy gap between the lowest excited state and the ground state

$$p_i h\nu_i = \Delta E \tag{7}$$

As mentioned above, this model is assumed to describe the decay rate from an idealized single level to the ground state. The fit of eq 5 to the data is shown as a solid line in Figures 10 and 11. Only the data above 150 K were used in the fitting process since the decay at the lower temperatures is assumed to be mainly radiative from a comparison of the relative intensities. Reasonable fits were obtained with three adjustable parameters, $\omega_{nr}(0)$, $h\nu_{accept}$, and p.

The results of these fits are also listed in Table IV. Note that, as before, E_{gap} refers to the energy separation between the observed onset of emission and excitation which can be accounted for in the Rh^{3+} compounds with the values of the promoting and accepting mode frequencies.

In the case of PtF_6^{2-} the gap was shown to be simply the sum of the two promoting modes. There the S factor of the emission band was shown to be about 6. For $RhCl_6^{3-}$ this factor cannot be determined as accurately. For $Cs_2NaInCl_6:Rh^{3+}$, Figure 4, we can see vibrational features more distinctly than for the others. Using their average spacing of 270 cm^{-1} and measuring from the peak back to the estimated origin at 11 300 − $h\nu_{promote}$ (from Tables II and V), we find nine intervals of 270 cm^{-1} to the peak, making $S \simeq 9$. This means that the first member of the series has an intensity about 1000 times less than the peak; thus it would be less than the signal/noise ratio in these experiments. By contrast, this ratio in PtF_6^{2-} is 80, making the first member much more detectable.

In the previous paragraph we used $h\nu_{accept} = 270$ instead of 320, the value obtained from the nonradiative decay rate. For such a crude model of the radiationless decay the rough agreement seems acceptable. Actually the anharmonicity would give a p_i value considerably higher than the one determined by the temperature dependence of the decay rate, and one would expect a smaller value of $h\nu_{accept}$ than 270, not a larger one.

An interesting feature of the emission spectrum in Figure 4 is the more distinct vibrational structure on the low-energy side of the band compared to the high-energy side. We had decided that the progression was in two modes ν_1 and ν_2 on the basis that the progression frequency is between these two, and by analogy to PtF_6^{2-}. The distinctness becomes a maximum near $n = 10$ or 11 and could be ascribed to the larger anharmonicity of the higher frequency which finally produces a peak at $n = 10$ equal to that of the lower less anharmonic mode. This behavior would fit the idea of an a_{1g} mode ν_1 of 280 cm^{-1} having an anharmonicity of $x = 2.5$ cm^{-1} with an e_g mode ν_2 of 223 cm^{-1} with no anharmonicity. Therefore, the observation of the changing distinctness of the structure on the emission bands supports the idea that ν_1 and ν_2 are both progression forming modes. When ν_2 forms a progression it means that there is a Jahn–Teller distortion in the upper state, as has been argued by Patterson for PtF_6^{2-}.[6]

The problems of the gap, and of the vibrational structure of the emission band can be discussed from a different viewpoint as illustrated by Zink and Reber in their treatment of the $PtCl_4^{2-}$ complex.[14]

The available vibrational data on the lattices in the present study and on another transition metal ion doped system, $Cs_2NaScCl_6:Mo^{3+}$, are summarized in Table V.[15] The effective promoting mode frequencies determined in this study are closest to ν_4 (t_{1u}), which, in fact, is the main promoting mode in the emission of PtF_6^{2-}. The effective accepting mode frequencies are near the average of $\nu_1(a_{1g})$ and $\nu_2(e_g)$ (300 vs 250 according to Tables IV and V). Further, it is not surprising that the vibronic progressions observed in the absorption and emission spectra correspond to the accepting modes. A relatively strong progression in these modes (a_{1g} and e_g) is possible since the electronic states involved have different electronic configurations and thus are expected to have different internuclear distances in both a_{1g} and e_g displacements.

Finally, from the S factor and the progression frequencies we can find an approximate size of the $RhCl_6^{3-}$ molecular ion in its $^3T_1(E)$ state. For $S = 10$ and $h\nu = 270$ in a symmetric mode, one finds a change of bond length, $\Delta b = 0.11$ Å. For $IrCl_6^{3-}$ with $s \approx 10.5$ and $\bar{\nu} = 340$ cm^{-1}, $\Delta b = 0.10$ Å. These values can be compared to the same transition in PtF_6^{2-} where $\delta b = 0.078$ Å.

Conclusion

We have studied the optical properties of Rh^{3+}- and Ir^{3+}-doped Cs_2NaMCl_6 (M = Y, In, Sc) in order to extend our knowledge of electronic structure of d^6 ions. Although the quality of the spectra obtainable from Rh^{3+} in Cs_2NaMCl_6 are not as resolved as for Pt^{4+} in Cs_2MF_6 it was possible to extract considerable information about the excited states by using all the data available and using analogies to the Pt^{4+} spectra.

A reasonable explanation of the energy gap between emission and absorption has been given. The geometrical change between ground and first excited state has been shown to be like that of PtF_6^{2-}. The temperature dependence of the emission lifetime showed that the promoting mode is probably ν_4 as in PtF_6^{2-}. The radiationless decay rate gave an accepting mode frequency near to the observed progression frequency.

Finally, a crystal field calculation for Rh^{3+} including spin–orbit coupling, fitted to the observed singlet and $^3T_1(E)$ positions, placed the $^3T_2$ band at the base of $^1T_1$ as suggested by the shoulder observed in the absorption spectra.

Acknowledgment. This research was supported by the National Science Foundation under research Grant No. CHE88-06365, and the W. R. Grace Corp. is thanked for a fellowship that supported S.C.W.

Registry No. $Cs_2NaScCl_6$, 28015-76-1; Cs_2NaYCl_6, 27880-16-6; $Cs_2NaInCl_6$, 32201-16-4; Rh^{3+}, 16065-89-7; Ir^{3+}, 22555-00-6.

(14) Zink, J. L.; Reber, C. *Coord. Chem. Rev.* **1991**, *111*, 1–14.
(15) Flint, C. D.; Paulusz, A. G. *Mol. Phys.* **1981**, *44*, 925.